



CHORUS

This is the accepted manuscript made available via CHORUS. The article has been published as:

Piezoelectric loss of superconducting microwave resonators integrated with thin-film lithium niobate

Likai Yang, Yuntao Xu, Chunzhen Li, Jiacheng Xie, Mohan Shen, and Hong X. Tang

Phys. Rev. Applied **20**, 054026 — Published 13 November 2023

DOI: [10.1103/PhysRevApplied.20.054026](https://doi.org/10.1103/PhysRevApplied.20.054026)

Piezoelectric loss of superconducting microwave resonators integrated with thin-film lithium niobate

Likai Yang,¹ Yuntao Xu,¹ Chunzhen Li,¹ Jiacheng Xie,¹ Mohan Shen,¹ and Hong X. Tang^{1,*}

¹*Department of Electrical Engineering, Yale University, New Haven, CT 06511, USA*

Thin-film lithium niobate (LN) has become an enabling platform in the development of quantum integrated circuits, for applications including microwave-to-optical converters and electro-mechanical transducers. Incorporation of high-quality planar superconducting resonators will further elevate the performance of these devices. However, alongside the desired interactions originated from LN, its piezoelectric nature also introduces parasitic coupling between microwave and phononic modes, resulting in excessive dielectric loss. In this work, we investigate such coupling by studying niobium nitride resonators directly deposited on patterned LN thin films. By varying device configuration, we pinpoint that overlapping electric field with LN can inadvertently excite bulk acoustic modes within the substrate, inducing microwave loss independent of the acoustic dissipation rate. The experimental results are supported by simulation and theoretical modeling. Our approach can be applied to different piezoelectric systems and provide insights into the design of microwave components for quantum transduction devices.

I. INTRODUCTION

Establishing coherent interfaces between different quantum systems is a key task in the development of future quantum networks. For example, microwave-to-optical transducers [1] enable mapping of quantum information from superconducting qubits to room-temperature optical links; electro-mechanical devices [2] can be used to study macroscopic quantum effects. As a material with favorable electro-optic, piezoelectric, and elasto-optic properties [3], lithium niobate (LN) draws great attention in the pursuit of these hybrid quantum systems. Recent advancement in nanofabrication of thin-film lithium niobate (TFLN) further enriches the system with high-quality, integrated optical [4] and mechanical [5] resonators, allowing better device performance and scalability. To date, electro-optic microwave-to-optical transducer with internal efficiency over 15 % [6] has been developed on TFLN; electro-mechanical resonator over 100 GHz [7] has also been demonstrated.

Planar superconducting resonators at microwave frequency are commonly used in the field of cavity quantum electrodynamics. Typically fabricated from thin-film aluminum [8], niobium [9], or niobium nitride (NbN) [10], these resonators can achieve quality factor (Q) over 1 million [11] and footprint as small as 100 μm [12]. The high quality factor and spatial confinement can significantly enhance the interaction between microwave mode and other quantum systems. Together with the flexibility to engineer their configuration according to different needs, superconducting resonators have become a versatile instrument for coupling to systems including superconducting qubits [13], solid-state spins [14], optical cavities [15], and bulk acoustic resonators [16].

Over recent years, multiple efforts have been made to integrate planar superconducting resonators with TFLN platform [17–19], aiming to realize efficient hybrid quantum interfaces. However, in these cases the resonator Q is usually limited to below 1 k, representing an over two-order-of-magnitude degradation compared to their intrinsic values. This extra loss

could originate from the strong piezoelectricity of LN, which induces unintentional coupling between microwave mode and phononic modes distributed in the substrate. Similarly, excessive dissipation of microwave field has also been observed with other piezoelectric materials such as thin-film aluminum nitride (AlN) [20, 21] and gallium arsenide (GaAs) [22]. Such discrepancy has emerged as one of the major bottlenecks in the optimization of device performance. Thus, there exists a pronounced need to investigate and model its underlying mechanism.

In this work, by depositing NbN resonators on TFLN patterned to different configurations, we study piezoelectricity induced microwave loss at GHz frequency. We show that Q is limited to ~ 200 for resonators on half-etch LN films, and identify the excitation of substrate thickness modes to be the major source of loss. By comparing substrate with flat and rough backside, we show that the induced loss is independent of the dissipation rate of mechanical modes. These results are then analyzed with simulation and theoretical modeling, demonstrating good agreements. The Q limitation improves to $\sim 10\text{k}$ when LN is patterned to full-etch waveguide structure and capacitively coupled to the resonator. Finally, in the case where magnetic field of the resonator overlaps with LN, the extra loss is suppressed. This scenario is of interest when accessing solid-state spins, such as rare earth ions [23, 24], doped in LN, and confirms that the extra loss arises from the interaction between electric field and mechanical modes. Our results can serve as a foundation for designing microwave components in piezoelectric systems and also provide insight on coupling microwave cavity with bulk acoustic resonators.

II. DEVICE

The schematic drawing of a representative superconducting resonator we study is shown in Fig. 1(a). 50 nm thick of NbN is first deposited on a dielectric substrate, e.g. high-resistivity silicon or sapphire, using atomic layer deposition (ALD). The resonator is then fabricated with electron beam lithography (EBL) and reactive ion etching (RIE). Detailed device fabrication and dimension can be found in Appendix A. The device can be modeled as a lumped-element LC resonator: the

* hong.tang@yale.edu

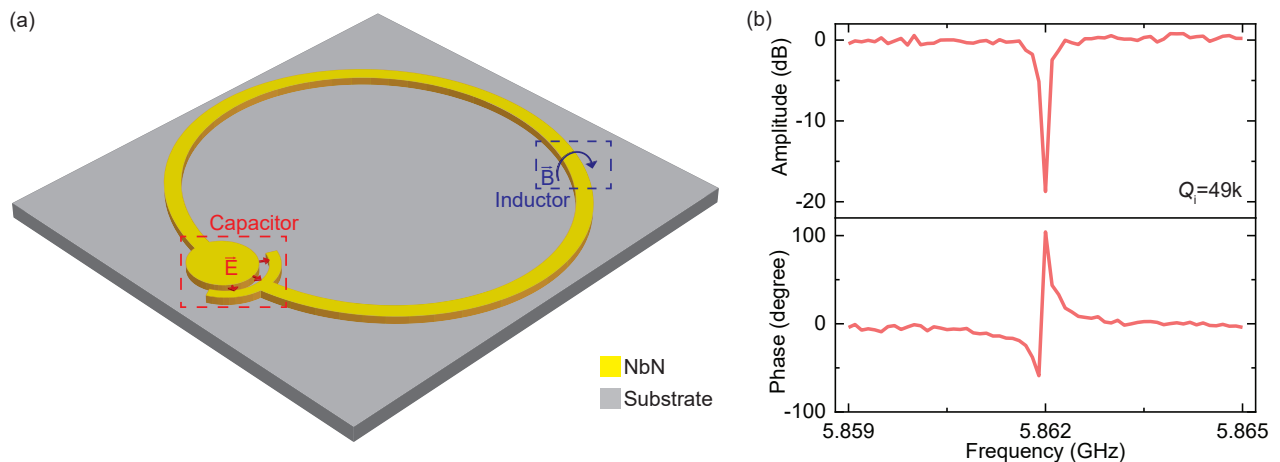


FIG. 1. (a) Schematic drawing of a representative superconducting resonator under study (not to scale). The device consists of 50 nm thick of NbN thin film deposited on a dielectric substrate (usually high-resistivity silicon or sapphire). It can be viewed as a lumped-element LC resonator, with the gap area as the capacitor and the loop wire as the inductor. (b) Spectrum of the resonator measured at 3 K. The resonance has an intrinsic Q of 49 k.

gap serves as the capacitor (C) to concentrate the electric field, while the magnetic field distributes along the loop wire which acts as the inductor (L). Such isolated distribution of electromagnetic field allows us to realize different coupling schemes with TFLN. Note that the resonator can be tailored to different shapes as long as the LC principle is obeyed and its frequency can be engineered by adjusting the value of capacitance and inductance.

After fabrication, the resonator is cooled down to 3 K and probed by a loop antenna. The reflection spectrum is plotted in Fig. 1(b), with a sharp resonance at 5.862 GHz exhibiting an intrinsic Q of 49 k. Based on this reference value, we then switch to study NbN resonators on patterned TFLN instead of simple dielectric substrate. The quality factor under different coupling configurations with LN are measured respectively and compared with the intrinsic value to extract the acoustic loss.

III. RESULTS

A. Half-etch lithium niobate

Half-etch slab waveguide structure is commonly used in TFLN to support guided optical mode for applications including microwave-to-optical transducers [18, 25] and electro-optic modulators [26]. In these devices, microwave components are coupled to the waveguide by overlapping the electric field with LN. To study the microwave loss in this scenario, we start with a 600 nm x -cut LN on insulator film and etch into it to form waveguides 350 nm high and 1.6 μm wide. The NbN resonator is then fabricated on the LN slab while the waveguide is put in the center of the capacitor to allow electric field coupling. A typical realization of this structure is sketched in Fig. 2(a), together with the electric field distribution in a cross section of the capacitor. Since the largest electro-optic coefficient of LN is $r_{33} = 34 \text{ pm/V}$ [3], here we consider the case where the electric field is mostly along z -direction of the crystal, which is of most interest for electro-optic applications.

Measurement results of the device at liquid helium temperature is shown in Fig. 2(b). When the backside of the substrate (2 μm silicon dioxide on 400 μm silicon) is flat, discrete dips corresponding to substrate acoustic modes can be seen in the spectrum, while the intrinsic Q of the resonator is limited to around 240. We then lap the backside of the device to achieve a rough surface and repeat the measurement. By increasing the acoustic dissipation rate, discrete dips in the spectrum are suppressed, as shown in Fig. 2(c). Yet, the overall linewidth of the microwave resonator remains similar. These results suggest that the microwave field can excite acoustic wave that traverses vertically through the substrate. At a flat backside, the wave gets reflected and forms standing wave modes with a constant free spectral range (FSR), i.e. the substrate acts as a bulk acoustic resonator. When the backside is rough, however, the excitation can be viewed as radiation into a continuum of phononic modes. The effective microwave loss induced by the coupling appears to be constant in two scenarios. Such coupling is modeled with 2D finite element simulation, as illustrated with the mechanical displacement and electric field distribution in Fig. 2(d). In the simulation, we analyze a simplified structure characterized by a reduced substrate thickness and a lateral dimension similar to the device. This approach enables us to gain insights into the mechanisms underlying the excitation of acoustic modes. Two different coupling schemes come into play here: the minor x -direction electric field can couple to the shear wave in the substrate through piezoelectric coefficient $e_{15} = 3.75 \text{ C/m}^2$ [27] of LN, while the dominant z -direction electric field can excite the longitudinal acoustic wave through $e_{31} = 0.2 \text{ C/m}^2$. Since $e_{15} \gg e_{31}$, the coupling to shear wave will be the major contributor, as confirmed by the simulation as well. Also, only anti-symmetric modes will be excited as the x -component of the electric field at two electrodes is opposite in direction.

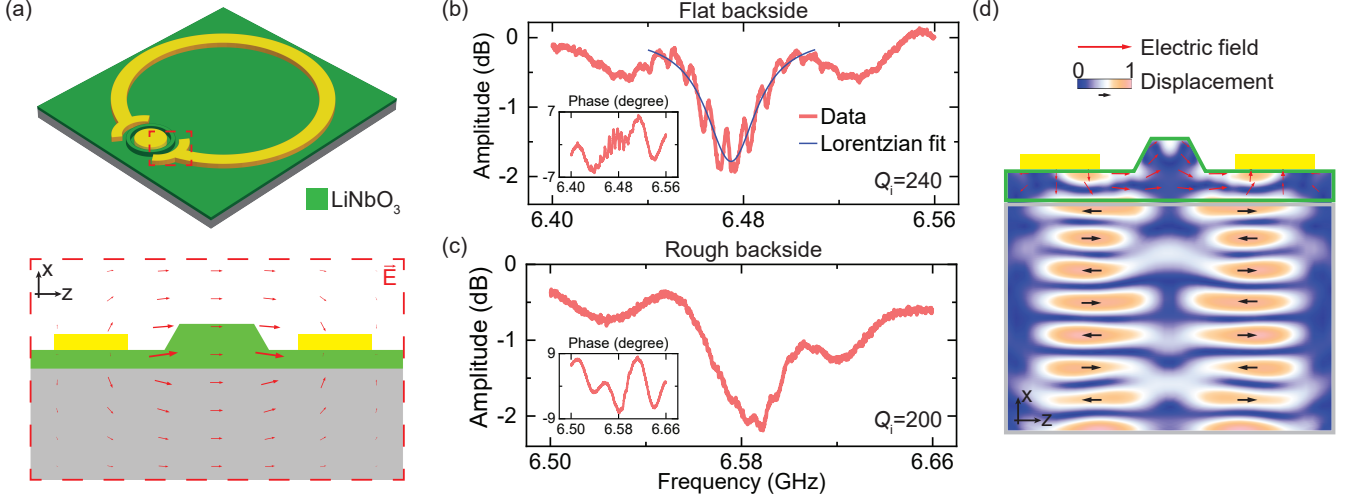


FIG. 2. (a) Schematic drawing of a NbN resonator on half-etch TFLN, with the capacitor coupled to a slab waveguide (not to scale). A cross section of the capacitor is also shown together with the distribution of electric field. (b) Measurement results of the microwave resonator at 4.2 K. When the backside of the substrate is flat, discrete dips can be seen in the spectrum suggesting the excitation of substrate acoustic modes. The effective intrinsic Q from Lorentzian fitting is 240. The phase response is also plotted in the inset. (c) After roughening the backside of the substrate, the acoustic modes are suppressed in the spectrum, but the microwave Q remains similar. (d) 2D simulation to demonstrate that the electric field can excite the shear wave in the substrate that travels in x -direction through piezoelectric constant e_{15} . The electric field and mechanical displacement is plotted.

B. Theoretical modeling

To quantify the piezoelectric microwave loss in previous measurements, we develop a theoretical model to describe the coupling. We start with the complex frequency response of the bare cavity [28]:

$$T(\omega) = 1 + \frac{-i\kappa_e}{(\omega - \omega_0) + i\kappa/2}, \quad (1)$$

where ω_0 is the resonance frequency and $\kappa = \kappa_e + \kappa_i$ is the total loss rate of the cavity. Here, κ_e is the external coupling rate and κ_i is the intrinsic loss rate of the bare cavity without piezoelectric coupling. The amplitude of the cavity reflection is then $|T(\omega)|^2$ which is in a Lorentzian shape. The coupling to bulk acoustic modes can be incorporated by considering a certain mode group (shear mode in the case above) with frequency $\omega_m^j = \omega_m + j \times \text{FSR}$, where $\omega_m \approx \omega_0$ is the center frequency for the mode group under consideration and j is the modal number. The loss rate and the electro-mechanical coupling rate of the acoustic modes are assumed to be constant at κ_m and g , respectively. This approximation is valid since the modal number of ω_m is much larger than the number of discrete acoustic modes in the span of the microwave resonance. The cavity response with the coupling can be rewritten as

$$T(\omega) = 1 + \frac{-i\kappa_e}{(\omega - \omega_0) + i\frac{\kappa}{2} - g^2 \sum_j \frac{1}{(\omega - \omega_m - j \times \text{FSR}) + i\kappa_m/2}}. \quad (2)$$

The equation is then used to fit the data in Fig. 2(b). The results are shown in Fig. 3(a). The model matches well with the measurement results, yielding $(\kappa_e, \kappa_i, \kappa_m, g, \text{FSR}) = 2\pi \times (2.1 \text{ MHz}, 4.5 \text{ MHz}, 4.0 \text{ MHz}, 4.7 \text{ MHz}, 7.9 \text{ MHz})$. Note that the intrinsic Q of the bare resonator is only around 1500 in

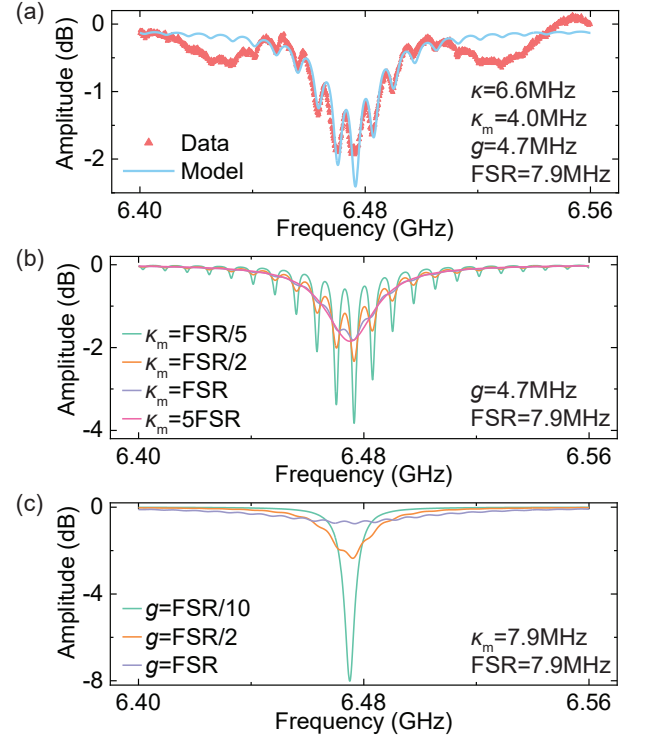


FIG. 3. (a) Measurement results and fitting using theoretical model, with the fitting parameters listed. The two curves show good agreements. (b) Cavity spectrum calculated from Eq. 2 with varying acoustic dissipation rate κ_m . Effective linewidth of the resonance stays unchanged. (c) Calculated spectrum with different electro-mechanical coupling rate g .

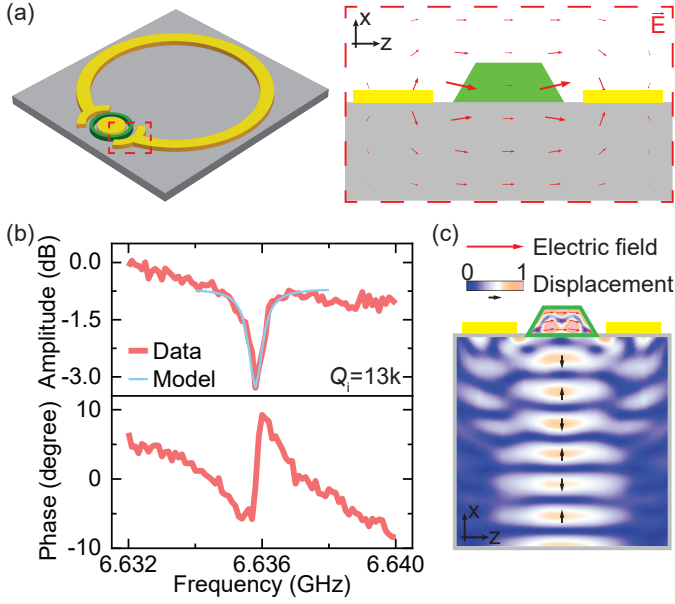


FIG. 4. (a) Schematic drawing of the device in which the NbN resonator is capacitively coupled to a full-etch LN waveguide (not to scale). The cross-sectional electric field distribution within the capacitor area is also shown. (b) Measurement results at 3 K. A piezoelectric limited intrinsic Q of 13 k is extracted. (c) 2D simulation of the structure demonstrating coupling to the longitudinal acoustic mode in the substrate. This arises from z -direction electric field and piezoelectric coupling coefficient e_{31} .

this case because the measurement is performed at an elevated temperature of 4.2 K. Still, the coupling to acoustic modes acts as the dominant loss channel, suggesting that the resonator Q will be limited to ~ 200 even at lower temperature. The coupling rate g is on the same order with the prediction from simulation (see Appendix C). The FSR of acoustic standing wave in the substrate can also be inferred from the sound velocity v and substrate thickness t as $\text{FSR} = v/2t$. Since the velocity for longitudinal wave in silicon is $v_l = 8430$ m/s and for shear wave $v_s = 5840$ m/s, we get $\text{FSR}_l = 10.5$ MHz and $\text{FSR}_s = 7.3$ MHz for 400 μm thick silicon. Our fitted value of $\text{FSR} = 7.9$ MHz is close to the shear wave FSR, supporting our assumption. The deviation might come from the variation in thickness or the hybridization with longitudinal wave.

A roughened backside can be treated in our model as an increased acoustic loss rate, or the regime where $\kappa_m \gtrsim \text{FSR}$. To quantify the cavity linewidth in this scenario, instead of treating the acoustic excitation as well-defined resonant modes, it can be approximated by a continuous distribution in the frequency domain with a constant density of state (DOS). With this representation, we can replace the summation in Eq. 2 with integration and arrives at (see appendix B)

$$T(\omega) \approx 1 + \frac{-i\kappa_e}{(\omega - \omega_0) + i\kappa/2 + i\pi g^2/\text{FSR}}. \quad (3)$$

Thus, the additional loss introduced by the electro-mechanical coupling can be extracted as $\kappa_{\text{add}} = 2\pi g^2/\text{FSR}$. This value is independent of κ_m and consistent with our observation.

Substituting the fitted value of g and FSR, we get $\kappa_{\text{add}} = 2\pi \times 17.6$ MHz, or a piezoelectric limited Q of 360, similar to our experimental results.

We can also plot how the cavity spectrum changes with varying parameters using Eq. 2. Keeping other variables constant, the spectrum with different acoustic dissipation rate κ_m is plotted in Fig. 3(b). As κ_m increases, the discrete acoustic modes in the spectrum are gradually suppressed, while the effective linewidth of the cavity remains unchanged. Fig. 3(c) demonstrates the cavity response when the electro-mechanical coupling g is varied. A notable increase in the cavity linewidth becomes evident as the coupling is enhanced.

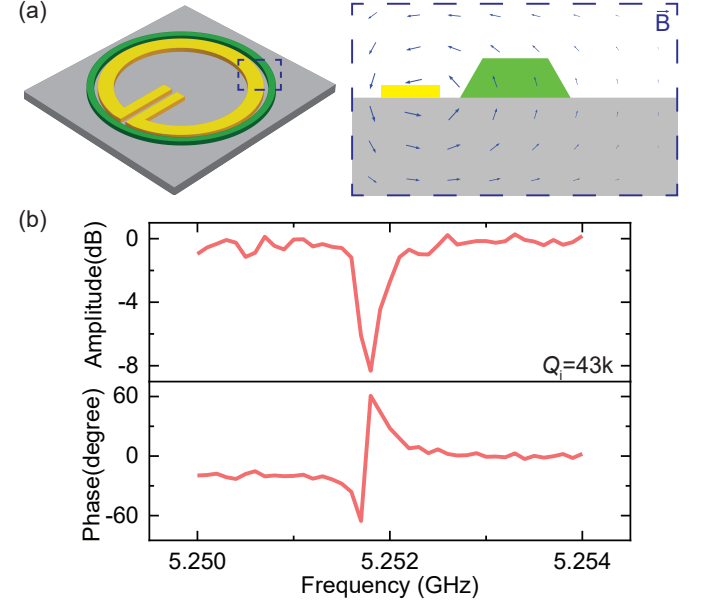


FIG. 5. (a) Schematic drawing of the NbN resonator inductively coupled to a full-etch LN waveguide (not to scale). In this case, the magnetic field component of the microwave mode overlaps with LN, as shown by the field distribution in the cross section of the loop wire. (b) Spectrum of the device at 3 K. The fitted intrinsic Q is 43 k, similar to the bare resonator, showing that the piezoelectric loss is suppressed.

C. Full-etch lithium niobate

Full-etch waveguide structure has also been developed on TFLN [29] and explored for electro-optic applications [6]. In this case, we consider NbN resonators deposited on the substrate and capacitively coupled to LN by putting the waveguide in the gap capacitor, as illustrated in Fig. 4(a). With NbN on the substrate, the electric field overlap with LN is substantially reduced since LN has a high dielectric constant ($\epsilon_{33} = 28$). Therefore, the electro-mechanical coupling is weakened resulting in higher microwave Q , at the expense of lower electro-optic coupling as well. The measurement result for this device at 3 K is shown in Fig. 4(b), with a fitted intrinsic Q of 13 k. Since the x -direction electric field in LN is largely suppressed by removing the slab, the excitation of longitudinal wave in the substrate emerges as a considerable source of loss as well. From simulation, we identify cou-

pling to both shear and longitudinal waves. The excitation of latter mode group is demonstrated in the field distribution of Fig. 4(c). Considering the 650 μm sapphire substrate used in this device, we get $g = 0.73$ MHz from the fitting using the theoretical model.

For the full-etch waveguide case, we can also engineer the configuration of NbN resonator so that its magnetic field overlap with LN instead of electric field. This is done by placing the waveguide along the loop wire of the NbN resonator, as sketched in Fig. 5(a). The cross section of the inductor shows the magnetic field distribution. The resonator spectrum measured at 3 K is plotted in Fig. 5(b). It exhibits an intrinsic Q of 43 k, similar to that of resonators on bare dielectric substrate. This result clearly suggests that piezoelectric loss is the major source of loss when integrating superconducting resonator with TFLN and supports our previous analysis. Such loss can be modified by varying the electric field overlap with LN in different device applications.

IV. CONCLUSION AND DISCUSSION

In conclusion, we have investigated piezoelectricity induced microwave loss for superconducting resonators integrated on thin-film lithium niobate platform by analyzing instances with different device configuration. Theoretical model and simulation methods are described in parallel to interpret the experimental results. We show that when the resonator is directly fabricated on half-etch LN, the electro-mechanical coupling is strong enough so that bulk acoustic shear modes in the substrate can be resolved in the microwave spectrum. By roughening the backside of the substrate, we further investigate the regime where the bulk acoustic modes approach the continuous limit and show that the microwave Q stays similar for both cases at around 200. By introducing a coupled-mode interpretation, we achieve good fitting of the experimental data and arrive at the acoustic loss formula $\kappa_{\text{add}} = 2\pi g^2/\text{FSR}$, with g as electro-mechanical coupling rate and FSR as the free spectral range of the target acoustic mode group. We then turn to study devices coupled to full-etch LN waveguides and observe an improved Q. In the case of magnetic field coupling, Q recovers to bare resonator limit of 50 k.

Different ways of improving microwave Q in thin-film piezoelectric systems can be readily implied from our results. The most intuitive method is to reduce the overlap between electric field and piezoelectric material. In more common cases where the desired interaction also arises from the electric field (such as electro-optics), doing so will lead to a trade-off in the target coupling strength. Our theoretical modeling then allows the fine-tuning of device design to locate the optimal point in parameter space. In the applications of addressing solid-state spins in piezoelectric material, the overlap with electric field should be minimized to suppress the parasitic loss. Furthermore, the device orientation can be engineered based on the anisotropy of the material. In LN, for example, the commonly-used z -direction electric field can excite acoustic modes through $e_{33} = 1.7$ C/m² and $e_{31} = 0.2$ C/m². Since the acoustic loss is proportional to $|e|^2$, such discrepancy in coupling coefficient could result in 70-fold change of piezoelectric loss for different film orientation. Follow-

ing the same principle, the stray electric field perpendicular to z -direction should be minimized in device design to avoid the largest piezoelectric coefficient e_{15} . The properties of the substrate used in thin-film platform also play a role in the acoustic loss. While choosing a material with large sound velocity could be helpful in terms of increasing the FSR, a simple thinning of the substrate might not be beneficial. This is because the electro-mechanical coupling g^2 is proportional to the overlap factor between electric field and mechanical mode, thus inversely related to the substrate thickness. Although the acoustic loss is independent of the mechanical dissipation in the discussed bad-cavity regime, improving mechanical Q can be helpful when the bulk mode FSR is much larger than both the microwave intrinsic linewidth and the mechanical mode linewidth. In this case, careful engineering of the microwave frequency or real-time frequency tuning can avoid the crossing between microwave and mechanical modes, thus reduce the extra loss. As a simple example, we can calculate the resonator spectrum using Eq. 2 with $(\kappa_m, g, \text{FSR}) = 2\pi \times (1 \text{ MHz}, 0.5 \text{ MHz}, 10 \text{ MHz})$ and $\kappa \ll \text{FSR}$. In this scenario, the piezoelectric Q limitation can range from 6 k when the resonance coincides with one of the acoustic modes ($\omega_0 = \omega_m$), to > 100 k when the resonance frequency is at the midpoint of adjacent acoustic modes ($\omega_0 = \omega_m + \text{FSR}/2$). When studying coherent coupling between microwave cavity and bulk acoustic resonator mediated by thin layer of piezoelectric material, similar procedures can also be implemented to maximize the coupling strength. Our results set a baseline for microwave resonator performance on TFLN and pave the way for device optimization in electro-mechanical quantum systems.

ACKNOWLEDGEMENT

We acknowledge funding support from the Air Force Office of Sponsored Research (AFOSR MURI FA9550-23-1-0338) and partial funding support from the Office of Naval Research on the development of nitride-based superconductors (under Grant No. N00014-20-1-2126). The part of the research that involves cryogenic instrumentation was supported by the US Department of Energy Co-design Center for Quantum Advantage (C2QA) under Contract No. DE-SC0012704. The authors would like to thank Dr. Yong Sun, Sean Rinehart, Lauren McCabe, Kelly Woods, and Dr. Michael Rooks for their assistance provided in the device fabrication. The fabrication of the devices was done at the Yale School of Engineering & Applied Science (SEAS) Cleanroom and the Yale Institute for Nanoscience and Quantum Engineering (YINQE).

APPENDIX A: DEVICE FABRICATION

The NbN superconducting resonator is fabricated using hydrogen silsesquioxane (HSQ) as mask. After electron beam exposure, the resist is developed with tetramethylammonium

hydroxide (TMAH) and the thin-film is subsequently etched in a RIE tool (Oxford 100) with fluorine based chemistry. Finally, the resist is removed with buffered oxide etch (BOE). The capacitor area of a typical device consists of electrodes 5 μm in width with a 10 μm gap. The length of the capacitor is around 150 μm . The loop wire inductor typically has width of 5 μm and radius around 500 μm .

Patterning of lithium niobate is done with same electron beam lithography process using HSQ. The etching is performed with pure argon (Ar) plasma and an additional step of RCA1 cleaning is adopted afterwards to remove the etching byproduct.

APPENDIX B: CAVITY COUPLED TO CONTINUOUS DISTRIBUTION OF MODES

In general, the reflection spectrum of a cavity coupled to a group of modes with distribution $\rho(\omega)$ can be written as [28]

$$T(\omega) = 1 + \frac{-i\kappa_e}{(\omega - \omega_0) + i\kappa/2 - \Gamma(\omega)}, \quad (\text{B1})$$

where

$$\Gamma(\omega) = G^2 \int_{-\infty}^{\infty} \frac{\rho(\omega') d\omega'}{\omega - \omega' + i\kappa_m/2} \quad (\text{B2})$$

and $G^2 = \sum g^2$ is the summation of coupling strength for all modes. In the case of discrete acoustic modes at ω_m^i with constant FSR, we have $\rho(\omega) = \frac{1}{n} \sum_i \delta(\omega - \omega_m^i)$. Here, we consider n modes in the span of the microwave resonance. Then, $G^2 = ng^2$ and

$$\Gamma(\omega) = g^2 \sum_i \frac{1}{\omega - \omega_m^i + i\kappa_m/2}. \quad (\text{B3})$$

The cavity spectrum then converges back to the formula of Eq. 2. For a continuum of phononic mode, the distribution can

be viewed as a rectangular function $\rho(\omega) = \frac{1}{\Delta}$ for $\omega_0 - \frac{\Delta}{2} < \omega < \omega_0 + \frac{\Delta}{2}$, with $\Delta \gg \kappa + \kappa_m$. The coupling strength is then $G^2 = \frac{\Delta}{\text{FSR}} g^2$. The integral can be calculated as

$$\Gamma(\omega) = \frac{2G^2}{i\Delta} \arctan\left(\frac{\Delta}{\kappa_m - 2i\omega}\right) \approx \frac{-i\pi G^2}{\Delta} = \frac{-i\pi g^2}{\text{FSR}}. \quad (\text{B4})$$

The effect of the coupling on the cavity can then be seen as an effective additional loss of $2\pi g^2/\text{FSR}$.

APPENDIX C: ELECTRO-MECHANICAL COUPLING RATE

The linear coupling rate between a microwave mode and a mechanical mode can be denoted by [30]

$$g^2 = \frac{1}{4} \omega \left(\int \vec{\eta}(\vec{r}) \cdot \overleftrightarrow{e} \cdot \vec{s}(\vec{r}) d\vec{r} \right)^2, \quad (\text{C1})$$

where $\vec{\eta}(\vec{r})$ and $\vec{s}(\vec{r})$ is the normalized electric field and strain tensor, respectively. \overleftrightarrow{e} is the coupling matrix. For the simplified case where the lateral dimension of the substrate is on the same order with the device, we can extract the field distribution from simulation and calculate the above integral. We arrive at $g \sim 1$ MHz for our half-etch device geometry, on the same order with the value fitted from experimental results.

In the practical case where the lateral dimension of the substrate is much larger than the device. The bulk acoustic resonator should be viewed as a multi-mode cavity. Each transverse mode can be represented by an in-plane wave vector k_{\perp} . The microwave field only couples effectively with the modes that have $k_{\perp} < \pi/d$ due to phase-matching condition, with d as the lateral dimension of the device. In our studied scenario where $2d$ is much larger than the acoustic wavelength, this effect can be approximated by a small spreading around acoustic center frequency ω_m^i . The coupling g is then the total coupling rate to these transverse modes and should stays similar for different size of substrate.

-
- [1] X. Han, W. Fu, C.-L. Zou, L. Jiang, and H. X. Tang, Microwave-optical quantum frequency conversion, *Optica* **8**, 1050 (2021).
- [2] B. Schriniski, Y. Yang, U. von Lüpke, M. Bild, Y. Chu, K. Hornberger, S. Nimmrichter, and M. Fadel, Macroscopic quantum test with bulk acoustic wave resonators, *Physical Review Letters* **130**, 133604 (2023).
- [3] R. Weis and T. Gaylord, Lithium niobate: Summary of physical properties and crystal structure, *Applied Physics A* **37**, 191 (1985).
- [4] M. Zhang, C. Wang, R. Cheng, A. Shams-Ansari, and M. Lončar, Monolithic ultra-high-q lithium niobate microring resonator, *Optica* **4**, 1536 (2017).
- [5] W. Jiang, R. N. Patel, F. M. Mayor, T. P. McKenna, P. Arrangoiz-Arriola, C. J. Sarabalis, J. D. Witmer, R. Van Laer, and A. H. Safavi-Naeini, Lithium niobate piezo-optomechanical crystals, *Optica* **6**, 845 (2019).
- [6] Y. Xu, A. A. Sayem, L. Fan, C.-L. Zou, S. Wang, R. Cheng, W. Fu, L. Yang, M. Xu, and H. X. Tang, Bidirectional interconversion of microwave and light with thin-film lithium niobate, *Nature communications* **12**, 4453 (2021).
- [7] J. Xie, M. Shen, Y. Xu, W. Fu, L. Yang, and H. X. Tang, Subterahertz electromechanics, *Nature Electronics* **6**, 301 (2023).
- [8] Z. Mineev, I. Pop, and M. Devoret, Planar superconducting whispering gallery mode resonators, *Applied Physics Letters* **103** (2013).
- [9] M. V. P. Altoé, A. Banerjee, C. Berk, A. Hajr, A. Schwartzberg, C. Song, M. Alghadeer, S. Aloni, M. J. Elowson, J. M. Kreikebaum, *et al.*, Localization and mitigation of loss in niobium superconducting circuits, *PRX Quantum* **3**, 020312 (2022).
- [10] A. Adamyan, S. Kubatkin, and A. Danilov, Tunable superconducting microstrip resonators, *Applied Physics Letters* **108** (2016).
- [11] A. Megrant, C. Neill, R. Barends, B. Chiaro, Y. Chen, L. Feigl, J. Kelly, E. Lucero, M. Mariantoni, P. J. O'Malley, *et al.*, Planar superconducting resonators with internal quality factors above one million, *Applied Physics Letters* **100** (2012).
- [12] M. Xu, R. Cheng, Y. Wu, G. Liu, and H. X. Tang, Mag-

- netic field-resilient quantum-limited parametric amplifier, *PRX Quantum* **4**, 010322 (2023).
- [13] A. Houck, J. Schreier, B. Johnson, J. Chow, J. Koch, J. Gambetta, D. Schuster, L. Frunzio, M. Devoret, S. Girvin, *et al.*, Controlling the spontaneous emission of a superconducting transmon qubit, *Physical review letters* **101**, 080502 (2008).
- [14] S. Wang, L. Yang, R. L. Cone, C. W. Thiel, and H. X. Tang, High-cooperativity coupling of rare-earth spins to a planar superconducting resonator, *Physical Review Applied* **18**, 014071 (2022).
- [15] C. Javerzac-Galy, K. Plekhanov, N. Bernier, L. D. Toth, A. K. Feofanov, and T. J. Kippenberg, On-chip microwave-to-optical quantum coherent converter based on a superconducting resonator coupled to an electro-optic microresonator, *Physical Review A* **94**, 053815 (2016).
- [16] X. Han, C.-L. Zou, W. Fu, M. Xu, Y. Xu, and H. X. Tang, Superconducting cavity electromechanics: the realization of an acoustic frequency comb at microwave frequencies, *Physical Review Letters* **129**, 107701 (2022).
- [17] P. Arrangoiz-Arriola, E. A. Wollack, M. Pechal, J. D. Witmer, J. T. Hill, and A. H. Safavi-Naeini, Coupling a superconducting quantum circuit to a phononic crystal defect cavity, *Physical Review X* **8**, 031007 (2018).
- [18] J. Holzgrafe, N. Sinclair, D. Zhu, A. Shams-Ansari, M. Colangelo, Y. Hu, M. Zhang, K. K. Berggren, and M. Lončar, Cavity electro-optics in thin-film lithium niobate for efficient microwave-to-optical transduction, *Optica* **7**, 1714 (2020).
- [19] T. P. McKenna, J. D. Witmer, R. N. Patel, W. Jiang, R. Van Laer, P. Arrangoiz-Arriola, E. A. Wollack, J. F. Herrmann, and A. H. Safavi-Naeini, Cryogenic microwave-to-optical conversion using a triply resonant lithium-niobate-on-sapphire transducer, *Optica* **7**, 1737 (2020).
- [20] L. Fan, C.-L. Zou, R. Cheng, X. Guo, X. Han, Z. Gong, S. Wang, and H. X. Tang, Superconducting cavity electro-optics: a platform for coherent photon conversion between superconducting and photonic circuits, *Science advances* **4**, eaar4994 (2018).
- [21] V. Jain, V. D. Kurilovich, Y. D. Dahmani, C. U. Lei, D. Mason, T. Yoon, P. T. Rakich, L. I. Glazman, and R. J. Schoelkopf, Acoustic radiation from a superconducting qubit: From spontaneous emission to rabi oscillations, *Physical Review Applied* **20**, 014018 (2023).
- [22] M. Scigliuzzo, L. E. Bruhat, A. Bengtsson, J. J. Burnett, A. F. Roudsari, and P. Delsing, Phononic loss in superconducting resonators on piezoelectric substrates, *New Journal of Physics* **22**, 053027 (2020).
- [23] S. Dutta, E. A. Goldschmidt, S. Barik, U. Saha, and E. Waks, Integrated photonic platform for rare-earth ions in thin film lithium niobate, *Nano letters* **20**, 741 (2019).
- [24] S. Probst, H. Rotzinger, S. Wünsch, P. Jung, M. Jerger, M. Siegel, A. Ustinov, and P. Bushev, Anisotropic rare-earth spin ensemble strongly coupled to a superconducting resonator, *Physical Review Letters* **110**, 157001 (2013).
- [25] L. Shao, M. Yu, S. Maity, N. Sinclair, L. Zheng, C. Chia, A. Shams-Ansari, C. Wang, M. Zhang, K. Lai, *et al.*, Microwave-to-optical conversion using lithium niobate thin-film acoustic resonators, *Optica* **6**, 1498 (2019).
- [26] M. Zhang, C. Wang, P. Kharel, D. Zhu, and M. Lončar, Integrated lithium niobate electro-optic modulators: when performance meets scalability, *Optica* **8**, 652 (2021).
- [27] S. Bouchy, R. J. Zednik, and P. Bélanger, Characterization of the elastic, piezoelectric, and dielectric properties of lithium niobate from 25° c to 900° c using electrochemical impedance spectroscopy resonance method, *Materials* **15**, 4716 (2022).
- [28] I. Diniz, S. Portolan, R. Ferreira, J. Gérard, P. Bertet, and A. Auffeves, Strongly coupling a cavity to inhomogeneous ensembles of emitters: Potential for long-lived solid-state quantum memories, *Physical Review A* **84**, 063810 (2011).
- [29] Y. Gao, F. Lei, M. Girardi, Z. Ye, R. Van Laer, J. Schröder, *et al.*, Compact lithium niobate microring resonators in the ultrahigh q/v regime, *Optics Letters* **48**, 3949 (2023).
- [30] M. Wu, E. Zeuthen, K. C. Balram, and K. Srinivasan, Microwave-to-optical transduction using a mechanical supermode for coupling piezoelectric and optomechanical resonators, *Physical review applied* **13**, 014027 (2020).